ELSEVIER

# Plagioclase preferred orientation by TOF neutron diffraction and SEM-EBSD

Yanxia Xie, Hans-Rudolf Wenk*, Siegfried Matthies[1]

*Department Earth and Planetary Science, University of California, Berkeley, CA 94720, USA*

## Abstract

The lattice preferred orientation (LPO) of an anorthosite (composed of andesine) sampled from a highly deformed anorthositic mylonite (Grenville Province, Quebec) was measured by TOF neutron diffraction and SEM-EBSD. The quantitative texture analysis of neutron data was accomplished by using the Rietveld texture analysis with the WIMV algorithm, implemented in the program package Materials Analysis Using Diffraction (MAUD). The texture calculations of the EBSD data were performed by using the program BEARTEX. Analyses from neutron and electron diffraction data gave similar results if EBSD data are smoothed to account for grain statistics. The principal pole figures show (010) roughly parallel to the rock foliation, (001) poles exhibiting a low angle ($\sim 25°$) to the pole to foliation, and (100) poles close to the $Y$-direction (perpendicular to the lineation and foliation pole). The [100] crystallographic direction shows a maximum in the lineation direction, [010] directions concentrate near the foliation pole. The geological deformation conditions and the constructed pole figure patterns indicate that the preferred orientation could be attributed to intracrystalline slip dominantly on (010) with [100] as slip direction. Elastic properties, calculated by averaging, document weak anisotropy that has implications for the seismic structure of the lower crust.

## 1. Introduction

The triclinic mineral plagioclase, which is abundant in the crust, has drawn much less attention to geologists interested in studying lattice preferred orientation (LPO) or texture than minerals as quartz, calcite or olivine, even though its chemistry and crystal structure have been studied extensively. The difficulty in measuring plagioclase LPO was the main reason for the lack of LPO research. Looking at the literature, almost all of the previous plagioclase LPO data reported relied on optical indicatrix axes measurements by time-consuming U-stage methods (e.g. Shelley, 1979, 1989; Suwa, 1979; Jensen and Starkey, 1985; Wenk et al., 1986; Kruhl, 1987; Olesen, 1987; Ji and Mainprice, 1988; Ji et al., 1988, 1994; Ague et al., 1990). The conventional X-ray method proved to be unsatisfactory for plagioclase, since its resolution is insufficient to separate the closely spaced or over-

* Corresponding author. Tel.: +1-510-642-7431.

*E-mail address:* wenk@seismo.berkeley.edu (H.-R. Wenk).

[1] Permanent address: Mueller-Berset-Str. 3, D-01309 Dresden, Germany.

lapped diffraction peaks, particularly because plagioclase often occurs together with other minerals. Higher resolution neutron diffraction was tried and pole figures were determined (Wenk et al., 1986), but at that time ODF calculations for triclinic crystals were not possible. The interpretation of deformation mechanisms of plagioclase was hindered by the small LPO database and by ambiguities of the data (Ji et al., 1994). Yet the study of plagioclase textures is important due to their geological and geophysical significance (e.g. Siegesmund et al., 1989; Siegesmund and Kruhl, 1991; Ji and Mainprice, 1988; Ji et al., 1988, 1997, 2000).

Plagioclase is regaining interest for texture geologists. In the last decade, the new technique of measuring the microtexture by scanning electron microscopy (SEM) has been applied to minerals. It is known as Electron Back Scatter Diffraction (EBSD) or Electron Back Scattered Patterns (EBSP). Its forerunner, SEM-SAC, has been applied to perthite crystallographic orientations (Pryer et al., 1995). Recently, albite preferred orientation in a greenschist-facies albite mylonite from a gabbro protolith was measured by EBSD (Prior and Wheeler, 1999). Synchrotron X-rays have been used to investigate the texture of experimentally deformed albite (Heidelbach et al., 2000). The neutron diffraction technique is also becoming accessible, particularly with the construction of new time-of-flight (TOF) diffractometers that are dedicated to texture research (Bennett et al., 1999; Ullemeyer et al., 1998). The first, and so far the only, application of the TOF neutron diffraction on a deformed amphibolite composed of low symmetry minerals hornblende (58%) and plagioclase (40%) was reported by Siegesmund et al. (1994), but no details in description of the quantitative texture procedure were given. Only recently, the developments of new software enable quantitative texture analysis of low symmetry minerals (Wenk et al., 1998). Plagioclase textures in a granodioritic mylonite were analyzed together with quartz and biotite by the WIMV algorithm from monochromatic neutron diffraction data (Chateigner et al., 1999). The rapidly developing advances in quantitative texture analysis make feldspars amenable for routine investigations and provide the background for a better understanding of the role of feldspars in the deformation of the lower crust.

The paper will add new data to the plagioclase texture literature. This report is the first application of the Rietveld texture analysis (Matthies et al., 1997; Lutterotti et al., 1997; Wenk et al., 2001) on the triclinic mineral plagioclase, based on the TOF neutron diffraction data, and it is the first report of EBSD texture analysis of andesine in an anorthositic mylonite. The neutron diffraction experiment was performed on the General Purpose Powder Diffractometer (GPPD) at the Intense Pulsed Neutron Source (IPNS) of Argonne National Laboratory, which uses white neutrons of a pulsed spallation source. The individual crystallographic orientation measurements were performed by a purely digital SEM-EBSD system at Berkeley (Wenk et al., 1999). Neutron data were analyzed using a texture analysis algorithm implemented in Rietveld software package MAUD (Lutterotti et al., 1999). In the following sections, experimental and analytical procedures for TOF neutron diffraction and EBSD will be described and results will be presented and discussed. We are emphasizing the analysis with TOF neutron diffraction and use EBSD more as a comparison. The effect of texture on elastic anisotropy of anorthosite is explored in a concluding section.

## 2. Experiments

### 2.1. Sample description

A roughly $7 \times 6 \times 5$ cm$^3$ rock block was sampled from a kilometer-wide anorthositic mylonite zone of the Morin Anorthosite Massif from Grenville Province in Quebec, Canada at a well-exposed waterfall locality of Riviere Odareau between Rawdon and Chertsey (For a tectonic description, readers are referred to Martignole, 1996). The hand specimen is composed of about 95% plagioclase and about 5% pyroxene, corresponding to sample MT-8 of Ji et al. (1994, 1997) with pervasive recrystallization and moderate preferred orientation. Plagioclase is light-grey, fine-grained mylonitic and its average composition is An50. Pyroxene is dark, elongated and concentrated in occasionally observed very thin ($\sim 1$ mm) layers. Foliation and lineation can be defined by the pyroxene layer and elongated pyroxene grains, respectively. Specimens for TOF neutron diffraction

and for EBSD were both cut from a pure plagioclase layer.

Optical microscope observations show the following microstructural features (Fig. 1): the anorthosite is recrystallized with an estimated average grain size of ~ 0.15 mm ranging from 0.002 to 0.4 mm. Most large grains are slightly elongated while small grains are roughly equant in shape (Fig. 1a). Grain boundaries are irregular. Large crystals are generally twinned, with undulatory extinction and bending (Fig. 1b), while small grains are more twin-free and have fewer deformation features.

The specimen preparations for neutron and EBSD experiments are not complicated. A cubic block of
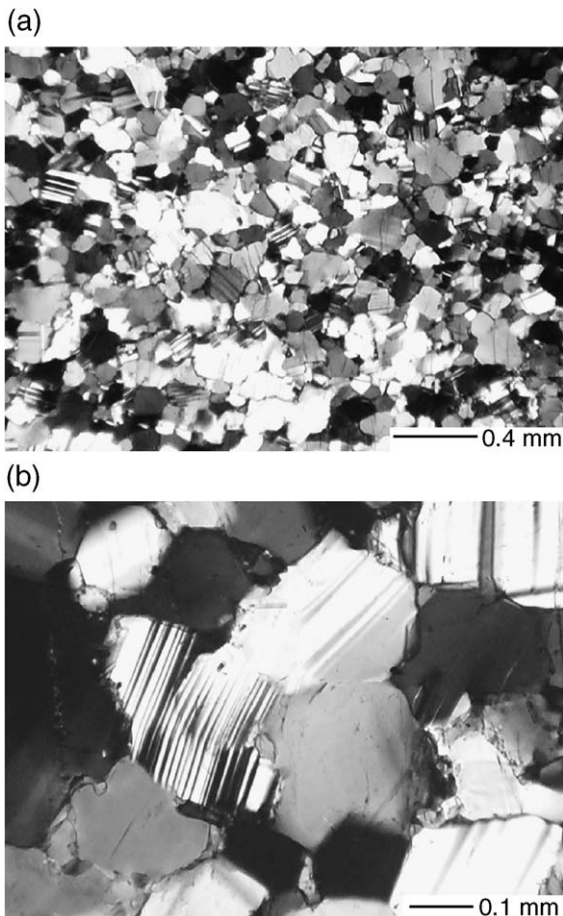


Fig. 1. Optical micrographs of anorthosite showing microstructures, crossed polars. (a) Overview picture. (b) Close view of crystals with twinning/bending/undulatory extinction features.

$1 \times 1 \times 1$ cm$^3$ was cut for neutron diffraction measurement. The corners and the edges of the cube were rounded to approximate a spherical shape and isotropic absorption. No further treatment was needed for the neutron specimen. The EBSD thin section was cut perpendicular to the foliation and parallel to the lineation. The mechanically polished thin section was additionally polished with colloidal silica (0.05 μm) for 24 h to remove surface damage. The specimen was not carbon-coated for better pattern quality.

## 2.2. TOF neutron diffraction

The GPPD at IPNS utilizes a pulsed source of spallation neutrons and applies TOF measurements (Jorgensen et al., 1989). The pulsed neutron source applies an electrical generator (Cockcroft-Walton) to generate intense bursts of protons at a repetition rate of 30 Hz. The protons are accelerated on their way to the target by a linear accelerator and a rapid cycling synchrotron. The accelerated protons strike a $^{235}$U target to release neutrons. The fast neutrons are slowed down by a liquid methane moderator maintained at 100 K. The moderated neutrons are directed down the flight path to the GPPD instrument and collimated to a size of $1.3 \times 5.0$ cm at the sample position, fully covering the 1-cm$^3$ specimen. The neutrons, with a flux of $3 \times 10^6$ neutrons cm$^{-2}$ s$^{-1}$ at the sample position, hit the sample and are diffracted into vertical detector tubes which are positioned on both sides of the sample within a horizontal plane at a constant radius of 1.5 m. Data from specific individual detector scattering angles are collected in detector banks and are successively accumulated in bins depending on the neutron flight time. The histograms constructed from these data provide the information used for the texture analysis. The high resolution is achieved by using a long incident flight path (20 m). GPPD has a total of 14 banks (Fig. 2a). In our analysis, we used data from 10 banks at average 2θ angles of $-144°$, $-126°$, $\pm 108°$, $\pm 90°$, $\pm 72°$, and $\pm 54°$. Data from scattering angles $\pm 30°$ were excluded due to their low resolution.

A locally designed Kappa-geometry goniometer, instead of a standard Eulerian-geometry goniometer, was used for the texture measurement. The Kappa-
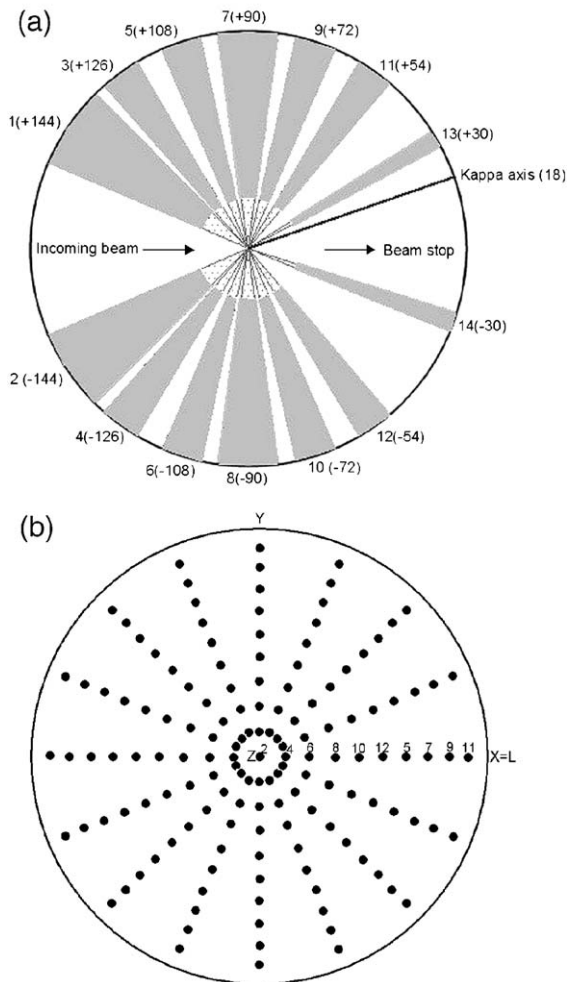
Fig. 2. (a) Arrangement of the IPNS-GPPD detector banks. The average angles of each banks (14 in total) and the rotation axis of the Kappa goniometer are indicated; (b) Pole figure coverage produced by the Kappa goniometer. The numbers indicate the detector banks (each of which covers a circle). The sample reference is also indicated: $X = L$ is the lineation direction; $Z$ is the normal to the foliation and $Y$ is perpendicular to $XZ$.

geometry allows the sample to rotate around omega, kappa, and phi axes. In our settings, kappa is fixed at 180° and omega at 18° (Fig. 2a). Only phi-motions are used for sample positioning. A total of 16 phi-rotations with an interval of 22.5° were sampled. The geometry produces the pole figure coverage shown in Fig. 2b. The reference sample orientations, lineation ($L$) direction $X$, the foliation normal direction $Z$, and

the direction $Y$ (normal to $XZ$) are indicated. In Fig. 2b, coverage from the 10 banks is indicated providing a total of 10 (banks) × 16 (sample orientations) = 160 individual spectra that are measured and used simultaneously in the texture analysis. To achieve sufficient counting statistics, the sample was measured for a total of 40 h with 2.5 h for each orientation.

### 2.3. SEM-EBSD

The SEM-EBSD system in Berkeley Texture Laboratory comprises a locally designed fully digital imaging system (fiber optic image transfer and a 14 bit Peltier-cooled 1 mega pixel CCD camera) attached to a Leo 430 SEM (Wenk et al., 1999). Associated software includes the Windows-based Leo SEM control, the locally designed package SEMTEX that drives motors, controls beam deflection and image acquisition, and interfaces with CHANNEL3+ that was used for pattern indexing (commercial software from HKL Software). The acquired data are then processed with the program BEARTEX (Wenk et al., 1998).

The specimen was mounted on a 70° tilted sample stage in the evacuated SEM sample chamber ($10^{-4}$–$10^{-6}$ Torr), with the rock lineation parallel to the SEM $X$-axis. Charging effects in the SEM were reduced by using a low accelerating voltage of 10 kV, beam current of 1.0 μA and a copper tape attached to the sample surface surrounding the measurement area. An area of $4 \times 4$ mm$^2$ was measured with a step size of 0.05 mm in both $X$ and $Y$ directions obtained by stage translation, resulting in a total of 6561 measured points. Back-scattered patterns were recorded on the phosphor screen attached to a fiber-optic light pipe that contained the CCD chip at the other end, outside the microscope. The CCD signal, collected on a $1024 \times 1024$ array, was electronically binned to $256 \times 256$. This signal was directly transferred to a PC for digital processing by subtracting the background pattern. Patterns such as the one shown in Fig. 3a were indexed (as shown in Fig. 3b) by CHANNEL3+, and orientation data were saved automatically in a file. The match unit for indexing is andesine (An 48) (with phase data provided by HKL Software). Indexing ambiguities were minimized through good specimen polishing and digital imaging with a large dynamic range (14 bits). Mis-indexing
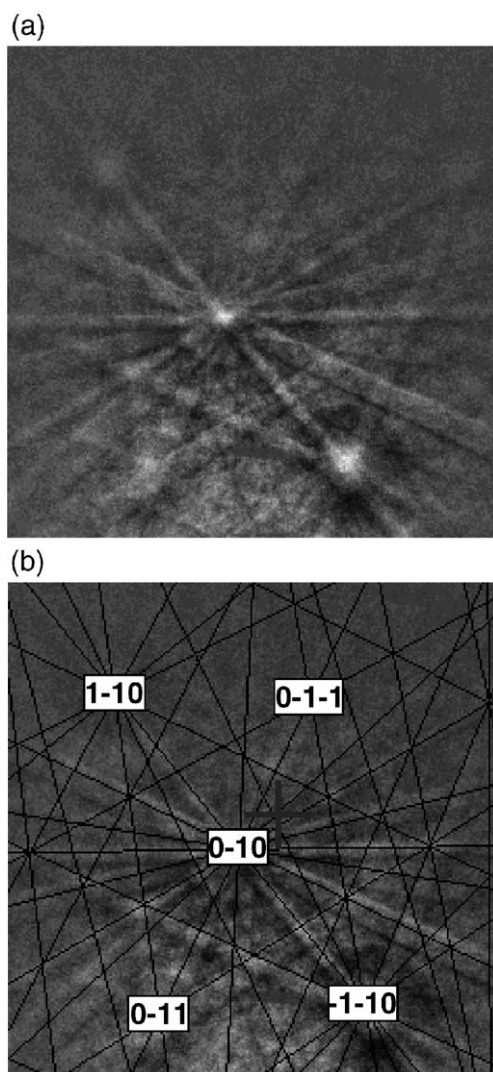
## (a)



## (b)



Fig. 3. (a) Digital background-subtracted EBSD pattern measured with a 14-bit 1 mega pixel CCD camera and 256 × 256 resolution, 10 kV. (b) Pattern in (a) is indexed by using the lines found by the Hough transform in (a) by CHANNEL3+.

problem was controlled by using a low Mean Angular Deviation (MAD between detected and simulated patterns) value of $1.2°$. Orientation angles would be rejected in the data file whenever MAD was greater than this control value (even with a high-quality pattern), which further assures the reliability of the EBSD measurement. Of the 6561 measurements, 934 (14%) could not be indexed or were excluded because of a high MAD index, resulting in a total of 5627

measurements that were used in the texture analysis. The same sample was measured twice and similar results were obtained. The whole measurement took about 17 h by using stage-scan mode.

### 2.4. Rietveld-texture analysis of neutron data

The raw neutron data from IPNS-GPPD were given to users in General Structure Analysis System format (GSAS, Larson and Von Dreele, 1986). Sixteen data files, recording the intensities at 16 sample orientations with 10 detector banks each, were input into a new analysis software package Materials Analysis Using Diffraction (MAUD, Lutterotti et al., 1999) for texture analysis.

Conventional neutron texture studies have relied on measuring a few pole figures at many sample orientations (between 500 and 1000, e.g. 700 in Wenk et al., 1994) as do X-ray pole figure measurements. In TOF neutron diffraction, intensities from all reflections are measured simultaneously as a function of time of flight at a fixed BRAGG angle, i.e. the experimental time is almost independent of the quantity of reflections that are recorded. This permits the TOF method to study efficiently the low symmetry or polyphase materials where large numbers of pole figures are necessary. This research has investigated the plagioclase texture through an approach of using many pole figures (56) and small number of sample orientations (160), compared to 650 in the Siegesmund et al. (1994) measurement, where only 21 pole figures had been considered.

Quantitative texture analysis was accomplished by the direct method WIMV implemented in MAUD. MAUD is a program package developed to analyze texture, residual stresses, microstrain as well as crystal structures, sample microstructures, and phase quantities, using diffraction spectra. It implements several texture analysis approaches into the Rietveld refinement method (Rietveld, 1969; Young, 1993), from basic March-Dollase, to Harmonic, WIMV, and Maximum Entropy. We chose to use the direct method WIMV due to its efficiency in separating texture from crystal structure, its advantage for low-symmetry compounds and composites with complicated diffraction spectra, and its elegance for TOF neutron diffraction, using small pole-figure regions and many diffractions (Lutterotti et al., 1997; Matthies et al.,

1988, 1997; Wenk et al., 2001). WIMV uses an iterative approach to determine the orientation distribution function (ODF) by evaluating the degree of the match between the calculated pole figures and the experimental pole figures, and correspondingly adjusting the estimated ODF until a satisfactory convergence is achieved.

Fig. 4 shows four spectra from four different sample orientations recorded at detector bank 5. Note that peak intensities at different sample orientations are different, illustrating the existence of texture. All 160 experimental spectra were input into MAUD for analysis. Besides the spectral data, we also need to provide the instrument (GPPD) parameter data and crystallographic data for andesine. These input data can be retrieved from databases.

First, the spectra from the 16 sample orientations were summed into a single histogram for each detector bank (totally 10). The summed spectrum minimizes

texture effects, but more importantly, it provides very good counting statistics. One sum spectrum is shown in Fig. 5 and peaks are indexed. Parameters that are fairly independent of texture (diffractometer geometry defined by three Caglioti parameters, profile asymmetry and two-theta offset, lattice parameters, background, and overall intensity factor) were refined based on these summed spectra for each detector. Table 1 shows result of refined lattice parameters for andesine and compares them with values from the literature.

Once a good fit between the calculated and the measured average spectrum was achieved, the original 160 spectra (using the d-spacing range 2–3.5 Å) were introduced and the texture mode (WIMV) was activated to combine the refinement of texture parameters together with the well-defined Rietveld parameters to perform the quantitative texture analysis. Texture weights were extracted for 56 reflections (with intensities exceeding 2%) by the Le-Bail
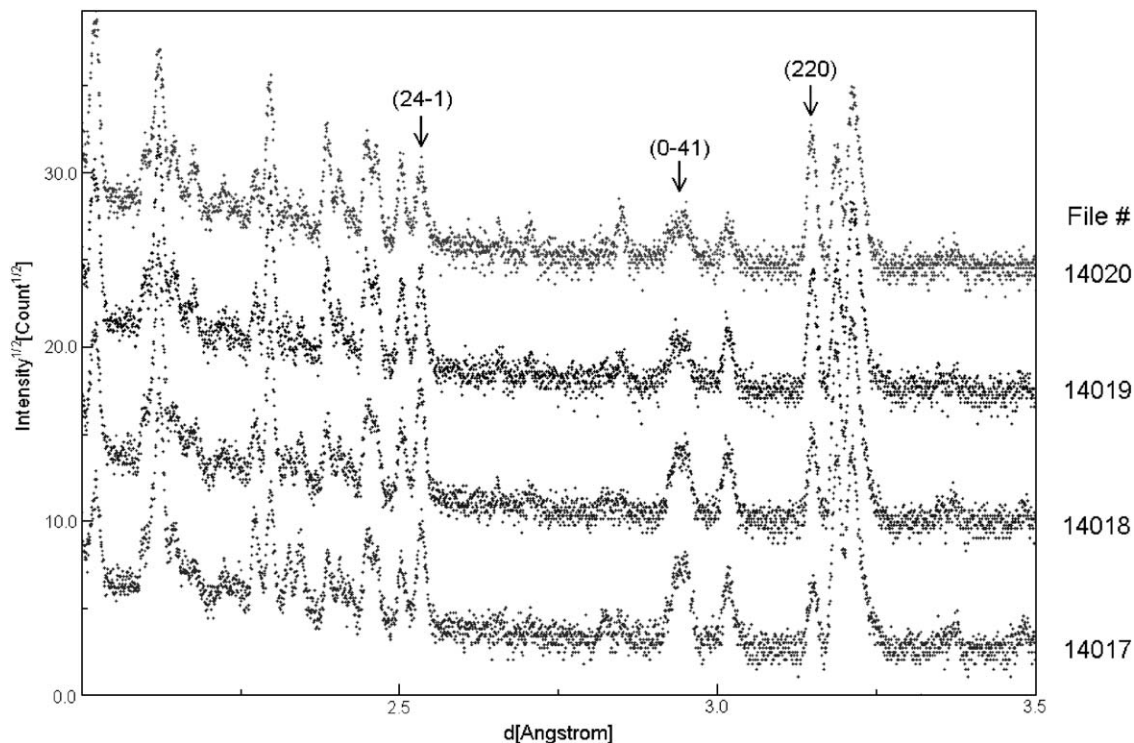


Fig. 4. TOF diffraction spectra from four different sample orientations recorded at detector bank 5. Note the relative intensities at different orientations are different. Numbers on the right side indicate the data file numbers corresponding to each sample orientations.
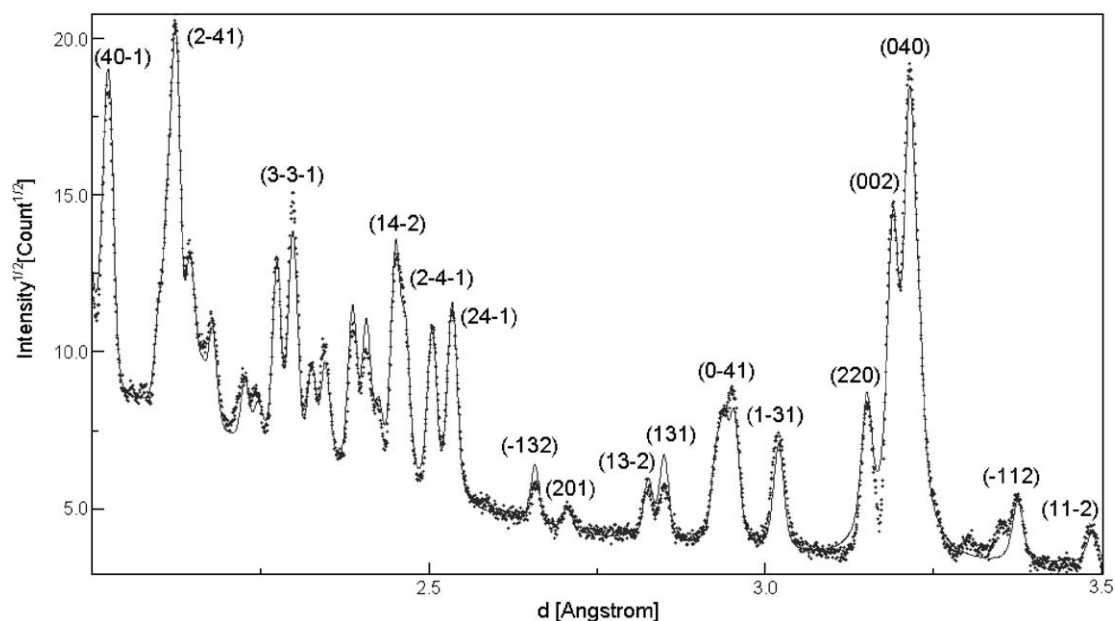
Fig. 5. The summed spectrum, averaged over the 16 sample orientations, at detector bank 7. The dotted line is the actual measurement. The solid line is the calculated spectrum. Important peaks are indexed.

algorithm (Matthies et al., 1997), weights were used to fill $5 \times 5°$ pole figure cells by triangulation (within 30°) and the resulting pole figures were used to obtain a first approximation of the ODF. Pole figures recalculated from the ODF were compared with the experimental ones. Appropriate corrections lead to the next ODF approximation. This procedure was repeated until convergence was reached. At the end of the iterations, the ODF and a suite of experimental and recalculated pole figures was output in MAUD and BEARTEX format. By using a Pentium III 700 MHz, 512 Mb RAM personal computer, it took a couple of minutes for one Rietveld refinement cycle and less than 1 h for the WIMV iteration.

Thirteen high intensity experimental pole figures with good matches were selected among the 56 MAUD-generated experimental pole figures. These 13 pole figures were analyzed further with the WIMV algorithm in BEARTEX (Wenk et al., 1998) for refining the ODF.

## 2.5. EBSD data analysis

The raw EBSD data with position, Euler angles, image quality, and match parameter were saved in Berkeley-EBSD format. Since SEM-EBSD measures the three-dimensional orientations directly, no complicated refinement procedure is involved here and data processing is straightforward. The 5627 individual

Table 1
Refined lattice parameters of andesine

| Data source | a (Å) | b (Å) | c (Å) | $\alpha$ | $\beta$ | $\gamma$ |
|---|---|---|---|---|---|---|
| This paper | 8.1824 (1) | 12.8807 (0) | 7.1227 (1) | 93.57 (3) | 116.24 (2) | 89.86 (4) |
| Bambauer et al. (1967) #91, An47.8 | 8.166 | 12.851 | 7.113 | 93.61 | 116.26 | 89.64 |

Estimated standard deviations are in parentheses. Data from literature are listed for comparison.

Table 2
The polar angles and azimuths (in degree) of the principal directions [100], [010], [001] and their corresponding pole approximations $(20\bar{1})$, (010), and $(\bar{1}02)$ in the Cartesian crystal coordinate system

| Direction | Polar angle | Azimuth | Pole | Polar angle | Azimuth |
|---|---|---|---|---|---|
| [100] | 116.2 | 0 | $(20\bar{1})$ | 124.6 | 0 |
| [010] | 93.6 | 91.7 | (010) | 90 | 90.0 |
| [001] | 0 | – | $(\bar{1}02)$ | 3.6 | 83.0 |

orientations were entered into $5 \times 5 \times 5°$ orientation space cells and the resulting ODF was normalized to express densities in multiples of a random distribution (m.r.d.) (INOR). The ODF was then smoothed by applying a Gauss bell of 18° full width at half maximum (SMOO). We will discuss later the reason for this choice of 18°. The principal pole figures (100), (010), and (001) were then calculated from the smoothed ODF

using PCAL and plotted using POXX. Fabrics of the principal crystallographic directions [100], [010], and [001] were indirectly obtained from calculations of the pole figures of (20$\bar{1}$), (010), and ($\bar{1}$02), respectively. For comparison, the polar angles and azimuths of these principal directions ([100], [010], and [001]) and their corresponding pole approximations (20$\bar{1}$), (010), and ($\bar{1}$02) are listed in Table 2.
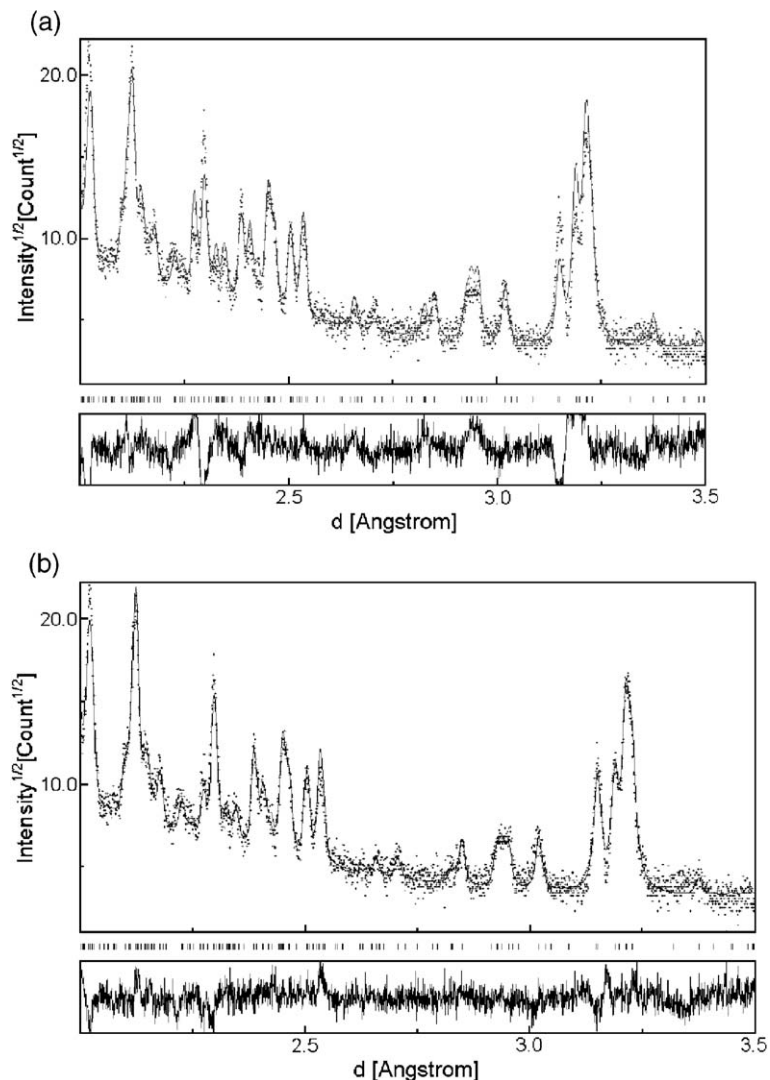


Fig. 6. (a) The Rietveld fit of a measured spectrum (at bank 7, file #14020, sample rotation angle Phi = 67.5) before applying texture correction. (b) The Rietveld fit of the same spectrum after the texture correction. The dotted curves represent the experimental data and the solid curves are the calculated spectra. The difference curves below the spectra illustrate deviations in intensity of the calculated from the observed.

## 3. Results

Fig. 6a gives an example of a Rietveld fit before applying texture correction of a measured spectrum at a specific sample orientation (phi = 67.5°) from the 90° detector bank (bank 7). The dotted curve represents the experimental data and the solid curve is the calculated spectrum. The difference curve below the spectrum illustrates deviations in intensity of the calculated from the observed. Fig. 6b shows the same spectrum fit but with the texture correction and deviations are efficiently reduced.

MAUD outputs a total of 56 pairs of experimental and recalculated pole figures in the d-spacing range 2–3.5 Å. We only show the first 14 pairs in Fig. 7 in the coordinate system of the neutron
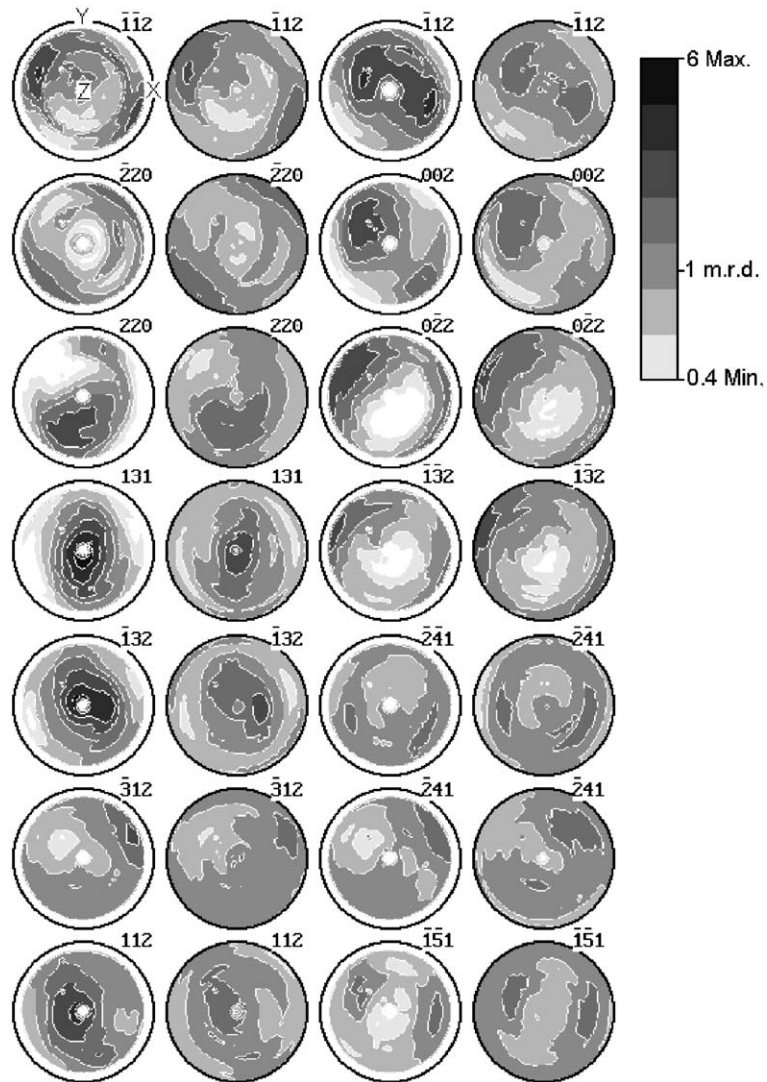


Fig. 7. 14 pairs of incomplete experimental (left) and recalculated pole figures (right) obtained with MAUD through Rietveld deconvolution. The pole density scale is shown on the right side. Log scale. Equal area projection. The rock lineation $X$ is in the W–E direction, $Y$ is in the N–S direction, and foliation pole $Z$ is in the center.

diffraction experiment with the pole to the foliation ($Z$) in the center and the lineation direction ($X$) to the right. Observe the remarkable match of the recalculated and experimental pole figures. Recalculated pole figures have slightly lower maximal pole densities.

The ODF, obtained using WIMV in BEARTEX from the 13 pole figures with best matches, was then rotated (program CSEC in BEARTEX) to conform with the standard setting used in structural geology, i.e. the pole to the foliation $Z$ on top and the lineation direction to the right. Principal pole figures (100), (010), and (001) and diagrams of crystallographic axes $[100] \approx (20\bar{1})$, $[010] \approx (010)$, and $[001] \approx (\bar{1}02)$ were then calculated from the rotated ODF (Fig. 8a).

The corresponding pole figures from EBSD are displayed in Fig. 8b. Notice the good agreement between the pole figures from neutron diffraction and EBSD. In all the pole figures, the lineation $X$ is in the W–E direction, $Y$ is in the center of the pole figures, and foliation pole $Z$ is in the vertical direction. (100) poles are close to the $Y$ direction. (010) pole maxima are located in the direction roughly perpendicular to the foliation. (001) poles exhibit a small angle ($\sim 25°$) to the pole to foliation. Crystallographic direction [100] has a maximum in the lineation direction $X$, [010] axes concentrate near the $Z$-direction.

## 4. Discussion

### 4.1. The reliability of the analysis

The quantitative texture analysis of triclinic plagioclase with diffraction methods has been a challenge, but the authors have now confidence in the results.

Traditional methods have relied on optical indicatrix axes measurements by time-consuming U-stage methods, depending on personal skills, and were therefore difficult to validate. Furthermore, the number of grains that can be measured is limited and grain statistics is poor. The high resolution, high penetration, and low absorption make neutrons suitable for bulk texture investigations of large sample volumes, and TOF neutrons are especially applicable for low symmetry and multiphase materials because many pole figures are required for a quantitative texture characterization (Wenk, 1994). In the case of Morin anorthosite, an estimated 300,000 grains were contained in a $1 \times 1 \times 1$ cm$^3$ sample with an average single grain volume of $0.15 \times 0.15 \times 0.15$ mm$^3$. In the d-spacing range of $2-3.5$ Å, 56 pole figures could be obtained. The efficiency and reliability of GPPD at IPNS for texture measurement has been previously tested with samples of deformed limestone (Lutterotti et al., 1997), as well as an eclogite composed dominantly of garnet and pyroxene (Wenk et al., 2001) and
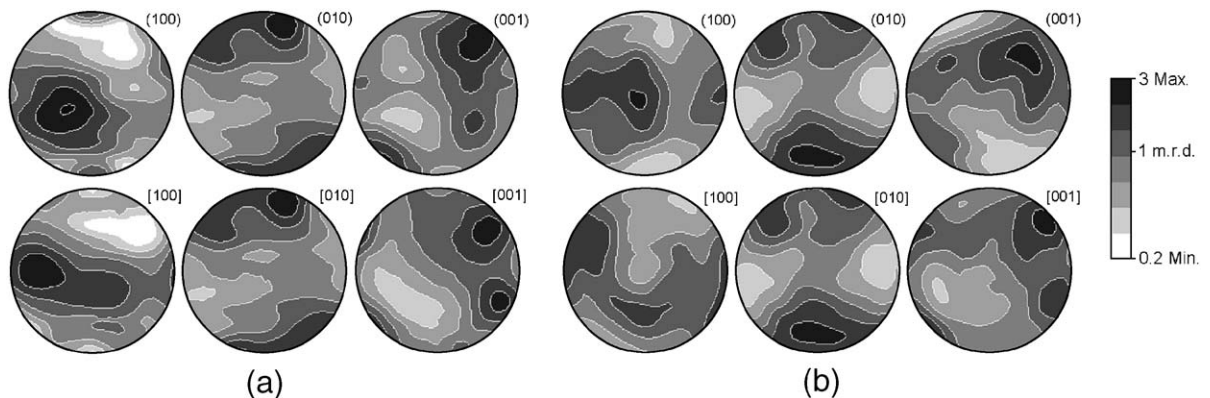


Fig. 8. The calculated principal pole figures and fabrics of crystallographic directions. (a) From neutron diffraction. (b) From SEM-EBSD (after smoothing with a 18° Gauss filter). In both (a) and (b), the rock lineation $X$ is in the W–E direction, $Y$ is in the center, and foliation pole $Z$ is in the N–S direction. The pole density scale is shown on the right side. Log scale. Equal area projection.

satisfactory results were obtained. The disadvantage of weak neutron diffraction was compensated by long measurement time, and the rather complex data processing was overcome by user-friendly analytical software packages, though both aspects need to be improved to make this a routine procedure.

We use the sample of anorthosite to compare more quantitatively neutron diffraction and EBSD. Fig. 8 illustrates excellent agreement but this has a caveat since it was only achieved after smoothing the data with an 18° Gauss filter. In the following paragraphs, we will evaluate statistical limitations of EBSD data.

EBSD is able to measure full orientations of individual grains directly and is an ideal technique for investigating relationships between texture and microstructure, as well as special misorientation relationships between neighboring grains. Its reliability depends on correct indexing, but by repeating measurements and by manual checks of individual measurements, we are confident that even for this triclinic mineral with a large unit cell overall results are correct. However, while 300,000 grains were involved in the neutron sample, EBSD measurements on the surface of the polished section (measurement area of $4 \times 4$ mm$^2$) covered at most 720 grains (through 5627 grid points). Statistics are therefore limited. Usually, this is expressed in exaggerated pole densities (Matthies and Wagner, 1996) and, while texture patterns are similar, EBSD pole densities are consistently higher than those obtained by neutron diffraction unless smoothing is applied.

A stochastic representation of a small number of single orientations in form of an ODF can be transformed into a more continuous form, changing the sharp spots of measured single orientations in the orientation space, by bell-like 3-dimensional Gaussians with a certain half-width $b$.

In the case of this plagioclase study, we have a statistically reliable ODF from the neutron experiment with a known texture sharpness. As a measure of texture strength, Bunge (1982) introduced the 'texture index' $F_2$. It is equal to the volume-averaged integral of squared orientation densities over the ODF and therefore mainly influenced by sharp peaks. The texture index is equal to 1.0 for a random texture. In the case of the neutron diffraction ODF, $F_2 = 3.0$ (Table 3).

In order to get comparable ODFs, we had to choose a smoothing width $b = 18°$ for the EBSD ODF to reduce the original ("stochastic") $F_2 = 96.8$ to $F_2 = 3$, corresponding to the neutron ODF (Table 3). The resulting pole figures from such a smoothed EBSD ODF are shown in Fig. 8b.

In general, the "true" texture sharpness is not known, if the ODF is determined from a limited number $N$ of EBSD-data, and consequently, the smoothing width is unknown. In the following section, we will explore, for anorthosite, the effect of number of measurements on texture strength.

There exists a critical limit $N_c$ of $N$ single orientations, below which an orientation distribution representation is meaningless. The $b(N)$-relation and the critical $N_c$ are sample-specific, depend on the crystal symmetry and the (unknown) orientation distribution of the sample. These relationships have been explored by Matthies and Wagner (1996, 1999), establishing the statistically exact asymptotic $1/N$ dependence of $F_2(N)$ for great $N$ (see also Van den Boogaart, 2002). For a sufficiently large number of orientations, this dependence can be used to determine the texture index $F_2$ of the sample and therefore the smoothing width $b$. In Fig. 9, the procedure of the $F_2$-determination is illustrated using the EBSD data of plagioclase. Even though in the present case, the number of

Table 3

Minima and maxima of ODF and the principal pole figures (in multiples of a random distribution), and the texture index (all calculations are performed in BEARTEX)

| Data source | Half-width ($b$) | ODF | | (100) | | (010) | | (001) | | Texture index |
|---|---|---|---|---|---|---|---|---|---|---|
| | | Min | Max | Min | Max | Min | Max | Min | Max | |
| Neutron | 0 | 0.000 | 51.430 | 0.255 | 2.782 | 0.441 | 2.232 | 0.324 | 2.284 | 3.058 |
| EBSD | 0 | 0.000 | 622.93 | 0.000 | 10.394 | 0.000 | 5.751 | 0.000 | 8.055 | 96.822 |
| | 5 | 0.000 | 413.21 | 0.008 | 8.706 | 0.023 | 5.023 | 0.047 | 6.003 | 42.508 |
| | 18 | 0.000 | 27.132 | 0.329 | 2.523 | 0.321 | 2.217 | 0.342 | 2.539 | 3.396 |

For EBSD determinations, effect of smoothing on pole densities is illustrated.
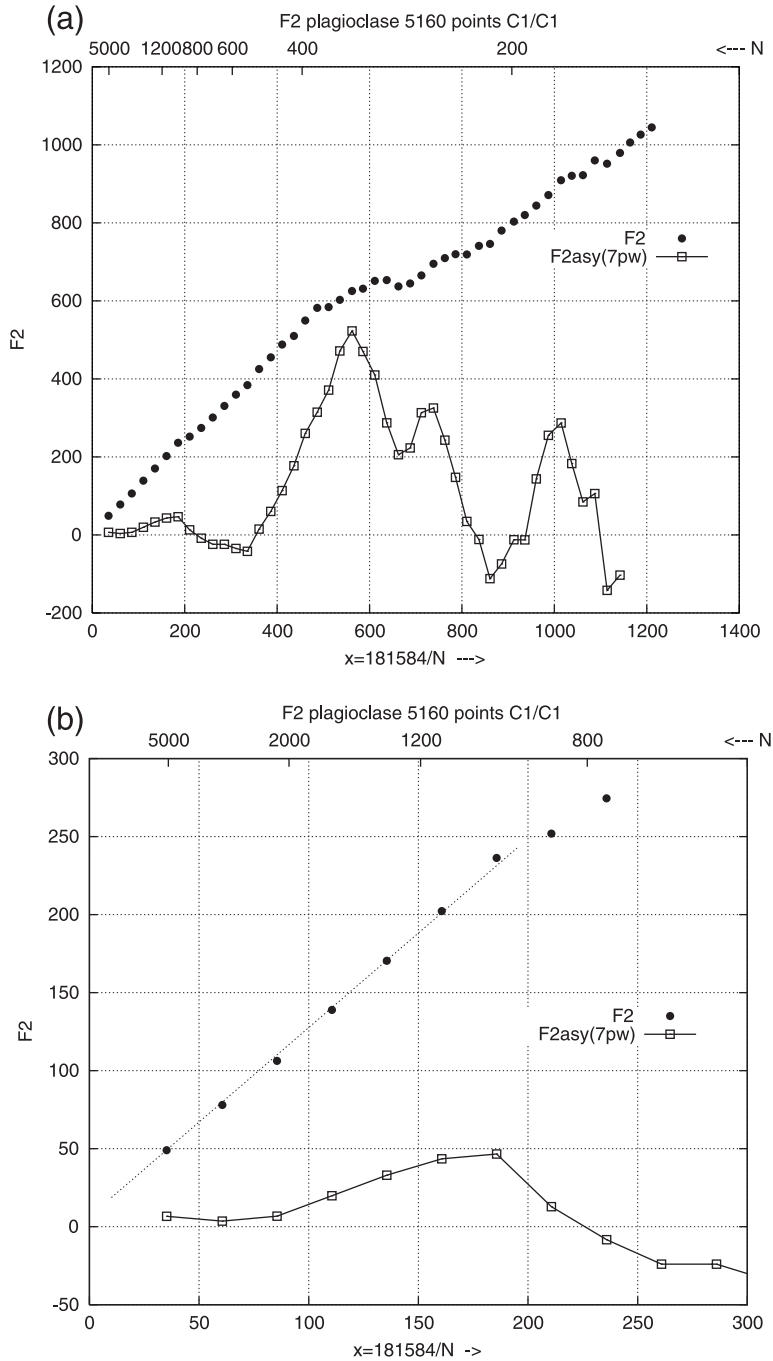
Fig. 9. Texture index $F_2$ as function of grain number $N$. (a) $F_2(x)$ and $F_2^{asy}(x)$ constructed using the EBSD data for anorthosite; (b) Detailed view of (a) at small $x$, $x = $ const$/N$, where the constant is the number of non-equivalent ODF cells.

measured orientations is not sufficient to determine $F_2 = 3$ satisfactorily, all qualitative properties of the $F_2$-dependence are well demonstrated.

Fig. 9a shows the dependence of $F_2$ as a function of increasing number of orientations (from right to left), using constant $1/N$-steps. As can be seen, $F_2$ decreases, first with stochastic oscillations, but for an increasing number of orientations more and more in a linear fashion. If this linear behavior becomes stable and the resulting straight line is extrapolated for infinite $N$, the intersection of this line at $x = 0$ with the $F_2$-axis provides the unknown texture coefficient $F_2$, without any other information about the texture of the sample. Indeed, as the enlarged portion of this diagram illustrates (Fig. 9b), the extrapolated intersection may be close to 3.0.

In Fig. 9, the $N$-dependence of $F_2$ is given as a function of the variable $x = \text{const}/N$. The number of non-equivalent orientation space cells is a reasonable value for const. For $5°$-cells and triclinic crystal symmetry, this number is large (181584). For the physically meaningful $N$, we have to take the number of the measured grains (in the given experiment of the order of 700) and not the number of measured EBSD-grid points (5627). In either case, the final $x$-values are much larger than 1 and the $F_2(x)$-curve has not really reached the stable linear dependence for a reliable estimate of $F_2$.

How many individual orientations are necessary to represent a texture, even with a poor resolution (large $b$)? The answer is, as soon as the $F_2(x)$-curve assumes a stable linear behavior. This stability can be examined by the character of the function '$F_2^{\mathrm{asy}}(x)$'. For each point $x$ and its 6 (or less) neighbours to the right, a straight-line can be fitted through the corresponding 7 (or less) $F_2(x)$-values. The intersection of this line with the $F_2$-axis at $x = 0$ gives the value of $F_2^{\mathrm{asy}}(x)$. For decreasing $x$ and a stable linear $F_2(x)$-behavior, the $F_2^{\mathrm{asy}}(x)$-curve will go from an oscillatory behavior into a horizontal line corresponding to the true value of $F_2$. $F_2^{\mathrm{asy}}(x)$ is also shown in Fig. 9. For $x < 86$, the oscillations become small and $F_2^{\mathrm{asy}}(x)$ reaches at least the right order of $F_2$: [$N = 2122$, $x = 86$, $F_2(86) = 103$, $F_2^{\mathrm{asy}}(86) = 6.8$; $N = 2998$, $x = 61$, $F_2(61) = 78$, $F_2^{\mathrm{asy}}(61) = 3.6$; $N = 5160$, $x = 35$, $F_2(35) = 49$, $F_2^{\mathrm{asy}}(35) = 6.6$]. This means starting from $x = 86$ ($N$ about 2000), in our case, an ODF-approximation becomes meaningful, though still only with a qual-

itative way, and considerably more orientations would be needed. The $F_2(x)$ and $F_2^{\mathrm{asy}}(x)$ criteria could be used in an EBSD scan to determine at which point data collection is sufficient to represent a texture. In most published EBSD texture analyses, this criterion is not applied, smoothing is done arbitrarily and results are, therefore, at best semiquantitative. In another case, where neutron and EBSD textures were compared, a 7.5 Gauss filter had to be applied to obtain comparable texture strength (Wenk et al., 1994). The width of the filter depends on texture type and number of individual orientations.

In neutron data analysis, the quality of the ODF is visually demonstrated by the good match of the recalculated pole figures and the observed pole figures (see Fig. 7). In EBSD analysis, the good pattern quality and a low indexing control value (MAD) assured the reliability of the individual orientation data. In addition, consistent results were obtained on the same sample with TOF neutron diffraction as well as EBSD and pole figures are in excellent agreement (Fig. 8). The LPO of plagioclase in an anorthosite mylonite sampled from the same geological area was measured with U-stage by Ji et al. (1994, 1997). Their (010), (100), [010], and [001] patterns are similar to ours. Yet, there are differences in (001) and [100] patterns that we cannot explain.

We conclude that, in spite of complexities with both methods, TOF neutron diffraction and SEM-EBSD can be used to reliably determine the texture of feldspars, if proper smoothing is applied to EBSD data, which requires either knowledge about the texture index or a very large number of individual orientation measurements.

### 4.2. Interpretation of the preferred orientation

The aim of this paper was to concentrate on developing methodology to measure textures of plagioclase in rocks, and demonstrating with an example that these methods are reliable. Nevertheless, a few comments on the texture interpretation are appropriate.

Deformation mechanisms of plagioclase at a variety of conditions are still poorly known. Experimental work by Tullis and Yund (1987) found that the plagioclase microstructure observed with the petrographic microscope exhibited ductile features resem-

bling those expected for dislocation creep, while transmission electron microscopy (TEM) showed evidence of microcracking and microscopic zones with cataclastic flow behavior over a wide range of conditions, suggesting that cataclastic flow is likely to be an important deformation mechanism. Olsen and Kohlstedt (1985) concluded, based on optical microstructure analysis combined with TEM observations, that intermediate plagioclase ($An_{25}$–$An_{48}$) subjected to extensive ductile deformation under low granulite facies conditions yielded primarily by intracrystalline slip and secondarily by mechanical twinning. Recovery processes started to appear under mid to upper amphibolite facies conditions. A recrystallized grain size piezometer for low-temperature recrystallization in feldspar was calibrated and reported by Post and Tullis (1999), but the applicability of the experimentally calibrated piezometer to naturally deformed rocks has yet to be verified.

Besides the uncertainty of the deformation mechanisms, understanding LPO patterns of plagioclase is equally challenging. Different mechanisms have been proposed. Texture may be due to geometrical rotations of elongated grains in a strain field (Shelley, 1979; Ague et al., 1990), or may be caused by oriented growth (Shelley, 1989). Under different conditions intracrystalline glide occurs (Jensen and Starkey, 1985; Olesen, 1987; Kruhl, 1987; Ji et al., 1988), or a combination of dislocation glide with mechanical twinning if grains are not anisotropic in shape (Ague et al., 1990). Dynamic recrystallization could also play an important role in LPO development (Ji and Mainprice, 1990). A general trend is to ascribe the LPO of plagioclase in metamorphic rocks to intracrystalline glide at high temperatures and to rigid body rotation at lower temperatures. Naturally, alignment of plagioclase prisms in volcanic rocks is a geometric effect during lava flow (Shelley, 1979).

In the case of the Grenville anorthosite mylonite, the high-grade granulite facies deformation condition (750–900 °C and 700–900 MPa; Zhao, 1997), the fairly equiaxed shape of the grains, and the pole figure patterns indicate that the preferred orientations can be attributed to intracrystalline slip, dominantly on (010) lattice planes which are parallel to the rock foliation. (001) has a low angle to the foliation, which may serve as a secondary slip plane, though this is more speculative. The slip direction is ambiguous as the

fabric of crystallographic directions was approximated from the closest (hkl) poles, though it is more likely that [100] could be the slip direction. (010) slip in the [001]/[100] direction is consistent with the easy slip law (Tullis, 1983). So far, most of the reports in the literature have suggested (010)[001] as the principal slip system responsible for the LPO patterns formed under the high-grade metamorphic (amphibolite and granulite facies) conditions (e.g. Olsen and Kohlstedt, 1984, 1985; Ji et al., 1988; Ji and Mainprice, 1988; Ague et al., 1990; Kruse and Stünitz, 1999; Kruse et al., 2001). (010)[100] slip has not been documented as an important deformation mechanism but recent experiments by Ji et al. (1999, 2000) suggest that there may be a transition from [001] to [100] slip with increasing deformation temperature.

However, while most of the discussion in the literature has emphasized deformation by slip, the sample analyzed in this study has been pervasively recrystallized and little is known about the effects of dynamic recrystallization on plagioclase preferred orientation.

### 4.3. Implications for seismic anisotropy of the lower crust

Plagioclase is volumetrically the most important mineral in the continental crust, constituting over 50%. It is particularly common in high-grade metamorphic rocks in the lower crust. Thus, the development of plagioclase LPO has been considered significant for interpreting seismic anisotropy of the lower crust.

The relationship between LPO and seismic properties is well established. If elastic properties of the single crystal are known (i.e. stiffness tensor $C_{ij}$), elastic properties of the textured aggregate are obtained by appropriate averaging over all orientations. In our case, we are using the geometric mean that is intermediate between Voigt and Reuss averages and close to the computationally much more complicated self-consistent micromechanical model (Matthies and Humbert, 1993). Once polycrystal elastic properties are known, seismic velocities (compressional-wave Vp and shear-wave Vs) can be calculated from the elastic average of the polycrystal. The computer program BEARTEX was used for all calculations.

Table 4

(left side) Single crystal elastic tensor of labradorite An53 (Simmons and Wang, 1971). (right side) Polycrystal elastic tensor obtained by geometric mean for the neutron texture (Voigt notation for $C_{ij}$, units: MPa)

| Single crystal | | | | | | Polycrystal | | | | | |
|---|---|---|---|---|---|---|---|---|---|---|---|
| 0.970 | 0.507 | 0.442 | 0 | − 0.096 | 0 | 1.166 | 0.510 | 0.492 | 0.008 | 0.003 | − 0.020 |
| | 1.629 | 0.370 | 0 | − 0.051 | 0 | | 1.178 | 0.494 | 0.002 | 0.006 | − 0.011 |
| | | 1.410 | 0 | − 0.150 | 0 | | | 1.147 | 0.006 | 0.001 | − 0.011 |
| | | | 0.196 | 0 | − 0.016 | | | | 0.330 | − 0.004 | − 0.002 |
| | | | | 0.330 | 0 | | | | | 0.335 | 0.0001 |
| | | | | | 0.370 | | | | | | 0.337 |

Table 4 lists the elastic constants of the single crystal used in our calculation and the geometric mean of the anorthosite mylonite, calculated from the neutron LPO. For a complete description of the elastic properties of the triclinic plagioclase, 21 independent elastic constants are required. All the data available in literature for feldspars have been reduced to monoclinic symmetry, which conveniently reflects the pseudo-monoclinic symmetry of plagioclase grains that show Albite and Pericline twinning. We used the monoclinic single crystal elastic constants of plagioclase An53, listed by Simmons and Wang (1971), based on data given by Ryzhova (1964). Aleksandrov et al. (1974) later made some modifications to Ryzhova's values but, in general, his set of $C_{ij}$ values has not changed significantly from Ryzhova's tabulation, except for two typing errors in $C_{23}$ and $C_{25}$ (Seront et al., 1993). An53 was chosen since it is the closest published composition to our studied sample. Maximum and minimum single crystal velocities (Vp, Vs1, and Vs2) calculated from these constants are given in Table 5 (In our notation, Vs2 is the faster shear wave.) and P-wave surfaces are shown in Fig. 10a.

Polycrystal velocities, calculated from the LPO of neutron data, are given in Fig. 10b and Table 5. The direct correlation of the pole figures (Fig. 8) with the P-wave surface (Fig. 10b) is difficult, considering the three dimensional nature of the texture. The fastest Vp is oblique to the foliation plane, which might be the result of the diffuse extension of the [010] maxima (the fastest Vp direction of the single crystal) to the left of the foliation pole, as well as a maximum of [001] (the intermediate Vp of the single crystal) located to the right of the lineation direction (see Fig. 8). While single crystals have a Vp anisotropy (Vmax − Vmin)/Vmax × 100%) of 27.5%, the anorthosite mylonite has a Vp anisotropy of only 3.28%. This value is very similar to the calculated (3.8%) and experimental (1.5%) values reported by Ji et al. (1997), in which Anisotropy=(Vmax − Vmin)/Vmean × 100% while Vmean=(Vmax + Vmin)/2) for their sample MT-8 from the same locality. It is much smaller than the anisotropy reported previously for plagioclase-containing rocks (e.g. Ji and Mainprice, 1988; Seront et al., 1993; Siegesmund et al., 1989; Siegesmund and Kruhl, 1991) and therefore significant in view of estimating anisotropy of the lower crust.

The weak anisotropy in spite of rather strong texture, may be specific for the sample that was analyzed, but it may also be influenced by specific features of the analysis. All previously reported values of plagioclase anisotropy were based on optical U-stage measurements with very limited statistics and Voigt averages. Our data relied on neutron diffraction LPO measurements, averaging over a large number of grains, and geometrical averages. Both aspects provide lower anisotropies.

Table 5

Maximum and minimum velocities of seismic waves (km s$^{-1}$), as well as anisotropy (Vmax − Vmin)/Vmax × 100%)

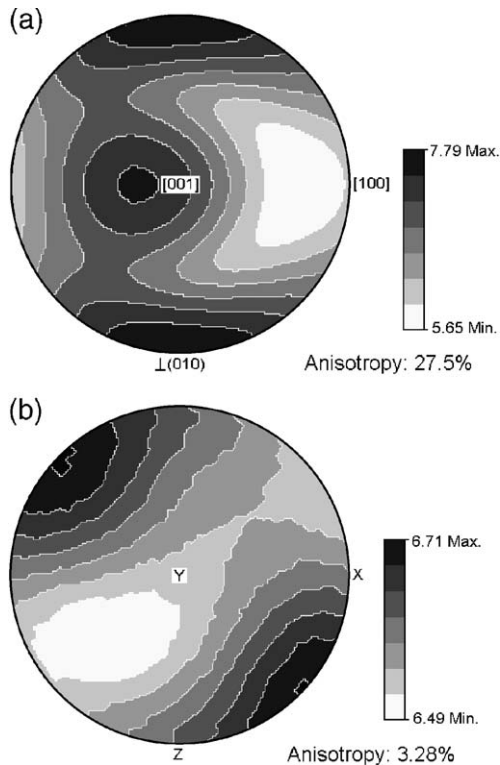| | Vp | | | Vs1 | | | Vs2 | | |
|---|---|---|---|---|---|---|---|---|---|
| | min | max | Anisotropy (%) | min | max | Anisotropy (%) | min | max | Anisotropy (%) |
| Single crystal | 5.65 | 7.79 | 27.5 | 2.69 | 3.61 | 25.5 | 3.39 | 4.66 | 27.3 |
| Polycrystal | 6.49 | 6.71 | 3.28 | 3.49 | 3.53 | 1.13 | 3.50 | 3.56 | 1.69 |

Fig. 10. (a) Calculated compressional wave Vp velocity surfaces (km/s) of plagioclase single crystal (An53). The elastic constants were referred to Simmons and Wang (1971); (b) Calculated Vp surfaces (km/s) of anorthosite mylonite from neutron diffraction texture data and geometric mean. The rock lineation $X$ is in the W–E direction, $Y$ is in the center, and foliation pole $Z$ is in the N–S direction. Linear scale. Equal area projection.

The unexpected low level of anisotropy for a polycrystalline sample with sharp texture, compared with the single crystal properties, can be understood by quantitatively analyzing in more detail the ODF of the given sample. The neutron-ODF in its original non-smoothed form shows a minimum $f(g)min = 0$ m.r.d. and a maximum $f(g)max \approx 50$ m.r.d., with a texture index equal 3 (Table 3). However, due to the statistical character of property averages, all orientations, including the random part, are of interest too. The level of a single crystal anisotropy can only be conserved for a polycrystalline sample if a few well concentrated preferred orientations contain overwhelming numbers of crystallites of the sample. In the present case, however, only about 3% of the orientation space are not occupied ($f(g) = 0$). Only

about 30% of orientation space has a frequency higher than the random level with $f(g) > 1$, involving only 45% of crystallites. They are concentrated in several preferred orientations with wide peaks. Only 14% of the orientation space is occupied with $f(g) > 2$ representing only 24% of all crystallites, and only 5.5% and 0.5% of all crystallites possess a frequency $f(g) > 5$ and $f(g) > 10$, respectively. From this, we infer that sharp texture maxima representative of small number of crystallites have not much influence on the macroscopic behavior of a sample. The important random component of a texture is always underestimated if grain statistics is poor.

## 5. Conclusions

Textures of triclinic minerals have been difficult to study, mostly restricted by the limited techniques suitable for deconvoluting complex diffraction spectra with overlapping diffraction peaks. This study presents a first successful TOF neutron study on plagioclase and shows the potential of the Rietveld method for texture analysis of low symmetry materials. The SEM-EBSD technique provided similar results, though grain statistics are obviously much worse and a true texture representation can only be obtained by adequate smoothing. In the Rietveld method, an iterative approach, which is capable of simultaneously refining texture and structure, can be extended to the simultaneous determination of structure, residual stress, strain, and texture, as well as phase proportions in polymineralic rocks (Wenk et al., 2001). By using personal computers and readily available user-friendly analytical software packages, this method is likely to add to a better understanding of deformation in complex metamorphic rocks.

# References

Ague, M.D., Wenk, H.R., Wenk, E., 1990. Deformation microstructures and lattice orientations of plagioclase in gabbros from Central Australia. Geophys. Monogr. 56, 173–186.

Aleksandrov, K.S., Alchikov, U.V., Belikov, B.P., et al., 1974. Velocities of elastic waves in minerals at atmospheric pressure and increasing precision of elastic constants by means of EVM. Izv. Acad. Sci. USSR, Geol. Ser. 10, 15–24.

Bambauer, H.U., Eberhard, E., Viswanathan, K., 1967. The lattice constants and related parameters of "plagioclases (low)". Schweiz. Mineral. Petrogr. Mitt. 47, 351–364.

Bennett, K., Von Dreele, R.B., Wenk, H.R., 1999. "HIPPO", a new high intensity neutron diffractometer for characterization of bulk materials. Proc. ICOTOM-12. NRC Research Press, Ottawa, pp. 129–134.

Bunge, H.-J., 1982. Texture Analysis in Materials Science—Mathematical Methods. Butterworths, London.

Chateigner, D., Wenk, H.R., Pernet, M., 1999. Orientation distributions of low symmetry polyphase materials using neutron diffraction data: application to a rock composed of quartz, biotite and feldspar. Textures Microstruct. 33, 35–43.

Heidelbach, F., Post, A., Tullis, J., 2000. Crystallographic preferred orientation in albite samples deformed experimentally by dislocation and solution precipitation creep. J. Struct. Geol. 22, 1649–1661.

Jensen, L.N., Starkey, J., 1985. Plagioclase microfabrics in a ductile shear zone from the Jotun Nappe, Norway. J. Struct. Geol. 7, 527–539.

Ji, S., Mainprice, D., 1988. Natural deformation fabrics of plagioclase: implications for slip systems and seismic anisotropy. Tectonophysics 147, 145–163.

Ji, S., Mainprice, D., 1990. Recrystallization and fabric development in plagioclase. J. Geol. 98, 65–79.

Ji, S., Mainprice, D., Boudier, F., 1988. Sense of shear in high-temperature movement zones from the fabric asymmetry of plagioclase feldspars. J. Struct. Geol. 10, 73–81.

Ji, S., Zhao, X., Zhao, P., 1994. On the measurement of plagioclase lattice preferred orientations. J. Struct. Geol. 16, 1711–1718.

Ji, S., Long, C., Martignole, J., Salisbury, M., 1997. Seismic reflectivity of a finely layered, graulite-facies ductile shear zone in the southern Grenville Province (Quebec). Tectonophysics 279, 113–133.

Ji, S., Jiang, Z., Wirth, R., 1999. Crystallographic preferred orientation (CPO) of experimentally sheared plagioclase aggregates: implications for crustal heterogeneity (abstract). EOS Trans. AGU Fall Meet. 80, F916.

Ji, S., Wirth, R., Rybacki, E., Jiang, Z., 2000. High-temperature plastic deformation of quartz-plagioclase multilayers by layer-normal compression. J. Geophys. Res. 105, 16651–16664.

Jorgensen, J.D., Faber, J., Carpenter, J.M., et al., 1989. Electronically focused Time-of-Flight powder diffractometers at the Intense Pulsed Neutron Source. J. Appl. Crystallogr. 22, 321–333.

Kruhl, J.H., 1987. Preferred lattice orientations of plagioclase from amphibolite and greenschist facies rocks near the Insubric Line (Western Alps). Tectonophysics 135, 233–242.

Kruse, R., Stünitz, H., 1999. Deformation mechanisms and phase distribution in mafic high-temperature mylonites from the Jotun Nappe, southern Norway. Tectonophysics 303, 223–249.

Kruse, R., Stünitz, H., Kunze, K., 2001. Dynamic recrystallization processes in plagioclase porphyroclasts. J. Struct. Geol. 23, 1781–1802.

Larson, A.C., Von Dreele, R.B., 1986. GSAS, General Structure Analysis System. Los Alamos National Laboratory Report LAUR86-748.

Lutterotti, L., Matthies, S., Wenk, H.R., Schultz, A.J., Richardson, J., 1997. Combined texture and structure analysis of deformed limestone from time-of-flight neutron diffraction spectra. J. Appl. Phys. 81, 594–600.

Lutterotti, L., Matthies, S., Wenk, H.R., 1999. Maud (material analysis using diffraction): a user friendly java program for Rietveld texture analysis and more. Proc. ICOTOM-12. NRC Research Press, Ottawa, pp. 1599–1604.

Martignole, J., 1996. Tectonic setting of anorthositic complexes of the Grenville Province, Canada. Petrology and Geochemistry of Magmatic Suites of Rocks in the Continental and Oceanic Crusts. Royal Museum for Central Africa, Tervuren, pp. 3–18.

Matthies, S., Humbert, M., 1993. The realization of the concept of the geometric mean for calculating physical constants of polycrystalline materials. Phys. Stat. Solidi, B 177, K47–K50.

Matthies, S., Wagner, F., 1996. On a 1/n law in texture related single orientation analysis. Phys. Stat. Solidi, B 196, K11–K15.

Matthies, S., Wagner, F., 1999. Using sets of individual orientations for ODF determination. Proc. ICOTOM-12. NRC Research Press, Ottawa, pp. 40–45.

Matthies, S., Wenk, H.R., Vinel, G.W., 1988. Some basic concepts of texture analysis and comparison of three methods to calculate orientation distributions from pole figures. J. Appl. Crystallogr. 21, 285–304.

Matthies, S., Lutterotti, L., Wenk, H.R., 1997. Advances in texture analysis from diffraction spectra. J. Appl. Crystallogr. 30, 31–42.

Olesen, N.O., 1987. Plagioclase fabric development in a high-grade shear Jotunheimen, Norway. Tectonophysics 142, 291–398.

Olsen, T.S., Kohlstedt, D.L., 1984. Analysis of dislocations in some naturally deformed plagioclase feldspars. Phys. Chem. Miner. 11, 153–160.

Olsen, T.S., Kohlstedt, D.L., 1985. Natural deformation and recrystallization of some intermediate plagioclase feldspars. Tectonophysics 111, 107–131.

Post, A., Tullis, J., 1999. A recrystallized grain size piezometer for

experimentally deformed feldspar aggregates. Tectonophysics 303, 159–173.

Prior, D.J., Wheeler, J., 1999. Feldspar fabrics in a greenschist facies albite-rich mylonite from electron backscatter diffraction. Tectonophysics 303, 29–49.

Pryer, L.L., Robin, P.F., Lloyd, G.E., 1995. An SEM electron-channeling study of flame perthite from the Killarney granite, southwestern Grenville Front, Ontario. Can. Mineral. 33, 333–347.

Rietveld, H.M., 1969. A profile refinement method for nuclear and magnetic structures. J. Appl. Crystallogr. 2, 65–71.

Ryzhova, T.V., 1964. Elastic properties of plagioclase. Bull. Acad. Sci. USSR, Geophys. Ser. 7, 633–635 (English Transl.).

Seront, B., Mainprice, D., Christensen, N.I., 1993. A determination of the three-dimensional seismic properties of anorthosite: comparison between values calculated from the petrofabric and direct laboratory measurements. J. Geophys. Res. 98, 2209–2221.

Shelley, D., 1979. Plagioclase preferred orientation, foreshore group metasediments, bluff, New Zealand. Tectonophysics 58, 279–290.

Shelley, D., 1989. Plagioclase and quartz preferred orientation in a low-grade schist: the roles of primary growth and plastic deformation. J. Struct. Geol. 11, 1029–1037.

Siegesmund, S., Kruhl, J.H., 1991. The effect of plagioclase textures on velocity anisotropy and shear wave splitting at deeper crustal levels. Tectonophysics 191, 147–154.

Siegesmund, S., Takeshita, T., Kern, H., 1989. Anisotropy of Vp and Vs in an amphibolite of the deeper crust and its relationship to the mineralogical, microstructural and textural characteristics of the rock. Tectonophysics 157, 25–38.

Siegesmund, S., Helming, K., Kruse, R., 1994. Complete texture analysis of a deformed amphibolite: comparison between neutron diffraction and U-stage data. J. Struct. Geol. 16, 131–142.

Simmons, G., Wang, H., 1971. Single Crystal Elastic Constants and Calculated Aggregate Properties: A Handbook, 2nd ed. The M.I.T. Press, Cambridge, MA.

Suwa, K., 1979. Plagioclase twin laws and fabrics in three specimens of anorthosite. Lithos 12, 99–107.

Tullis, J., 1983. Deformation of feldspars. In: Ribbe, P.H. (Ed.), Feldspar Mineralogy, 2nd ed. Reviews in Mineralogy, vol. 2. Mineral. Soc. Am., pp. 297–323.

Tullis, J., Yund, R.A., 1987. Transition from cataclastic flow to dislocation creep of feldspar: mechanisms and microstructures. Geology 15, 606–609.

Ullemeyer, K., Spalthoff, P., Heinitz, J., Isakov, N.N., Nikitin, A.N., Weber, K., 1998. The SKAT texture diffractometer at the pulsed reactor IBR-2 at Dubna: experimental layout and first measurements. Nucl. Instrum. Methods Phys. Res., A 412/1, 80–88.

Van den Boogaart, K.G., 2002. Statistics for Individual Crystallographic Orientation Measurements. PhD Thesis, Bergakademie Freiberg, Germany; Shaker Verlag, Aaachen. 159 pp.

Wenk, H.R., 1994. Texture analysis with TOF neutrons. In: Joergensen, J.D., Schultz, A.J. (Eds.), Time-of-Flight Diffraction at Pulsed Neutron Sources. Trans. Am. Cryst. Assoc., vol. 29, pp. 95–108.

Wenk, H.R., Bunge, H.J., Jansen, E., Pannetier, J., 1986. Preferred orientation of plagioclase-neutron diffraction and U-stage data. Tectonophysics 126, 271–284.

Wenk, H.R., Pawlik, K., Pospiech, J., Kallend, J.S., 1994. Deconvolution of superposed pole figures by discrete OD methods: comparison of ADC and WIMV for quartz and calcite with trigonal crystal and triclinic specimen symmetry. Textures Microstruct. 22, 233–260.

Wenk, H.R., Matthies, S., Donovan, J., Chateigner, D., 1998. BEARTEX: a windows-based program system for quantitative texture analysis. J. Appl. Crystallogr. 31, 262–269.

Wenk, H.R., Donovan, J., Xie, Y., Johnson, G.C., Toker, E., 1999. Texture analysis with a digital SEM-EBSD system. Proc. ICOTOM-12. NRC Research Press, Ottawa, pp. 235–240.

Wenk, H.R., Cont, L., Xie, Y., Lutterotti, L., Ratschbacher, L., Richardson, J., 2001. Rietveld texture analysis of Dabie Shan eclogite from TOF neutron diffraction spectra. J. Appl. Crystallogr. 34, 442–453.

Young, R.A., 1993. The Rietveld Method. Oxford Univ. Press, New York.

Zhao, X.O., 1997. Microstructure et petrofabrique des minéraux à haute température: example du terrain du Morin, Province de Grenville, Québec. PhD Thesis, Université de Montréal, Canada.